Topologically nontrivial and trivial zero modes in chiral molecules

Xiao-Feng Chen [1,2] Wenchen Luo,[1] Tie-Feng Fang,[3] Yossi Paltiel,[4] Oded Millo,[5] Ai-Min Guo [1,*] and Qing-Feng Sun[6,7,8]

[1]*Hunan Key Laboratory for Super-microstructure and Ultrafast Process, School of Physics and Electronics,*
Central South University, Changsha 410083, China
[2]*School of Physical Science and Technology, Lanzhou University, Lanzhou 730000, China*
[3]*School of Sciences, Nantong University, Nantong 226019, China*
[4]*Applied Physics Department and the Centre for Nanoscience and Nanotechnology,*
The Hebrew University of Jerusalem, 91904 Jerusalem, Israel
[5]*Racah Institute of Physics and the Centre for Nanoscience and Nanotechnology,*
The Hebrew University of Jerusalem, 91904 Jerusalem, Israel
[6]*International Center for Quantum Materials, School of Physics, Peking University, Beijing 100871, China*
[7]*Hefei National Laboratory, Hefei 230088, China*
[8]*CAS Center for Excellence in Topological Quantum Computation, University of Chinese Academy of Sciences, Beijing 100190, China*

Recently, electron transport along chiral molecules has been attracting extensive interest and a number of intriguing phenomena have been reported in recent experiments, such as the emergence of zero-bias conductance peaks in the transmission spectrum upon the adsorption of single-helical protein on superconducting films. Here, we present a theoretical study of electron transport through a two-terminal single-helical protein sandwiched between a superconducting electrode and a normal-metal one in the presence of a perpendicular magnetic field. As the proximity-induced superconductivity attenuates with the distance from superconducting media, the pairing potential along the helix axis of the single-helical protein is expected to decrease exponentially, which is characterized by the decay exponent λ and closely related to the experiments. Our results indicate that (i) a zero-bias conductance peak of $2e^2/h$ appears at zero temperature and the peak height (width) decreases (broadens) with increasing temperature, and (ii) this zero-bias peak can split into two peaks, which are in agreement with the experiments [see, e.g., H. Alpern *et al.* Nano Lett. **19**, 5167 (2019)]. Remarkably, Majorana zero modes are observed in this protein-superconductor setup in a wide range of model parameters, as manifested by the Z_2 topological invariant and the Majorana oscillation. Interestingly, a specific region is demonstrated for decaying superconductivity, where topologically nontrivial and trivial zero modes coexist and the bandgap remains constant. With increasing the pairing potential, the topologically nontrivial zero modes will transform to the trivial ones without any bandgap closing-reopening, and the critical pairing potential of the phase transition attenuates exponentially with λ. Additionally, one of the two zero modes can be continuously shifted from one end of the protein toward the other end contacted by the normal-metal electrode. The underlying physics of the topologically nontrivial and trivial zero modes is discussed.

I. INTRODUCTION

Majorana fermion, firstly predicted to be one fundamental particle by Ettore Majorana in 1937 [1], was considered as an excitation in condensed matter physics. Unpaired Majorana fermions were reported on vortices of chiral two-dimensional *p*-wave superconductors [2–5]. Kitaev put forward a seminal model to detect such exotic particles at the two ends of a nanowire, which may facilitate realizing half-qubits in topological quantum computing schemes [6]. Since then, a number of one-dimensional (1D) systems were proposed to observe Majorana fermions or Majorana zero modes, such as ultracold fermionic atoms with spin-orbit interaction [7], quantum dot chains [8,9], helical Shiba chains [10,11], and ferromagnetic atomic chains on superconducting substrates [12–16]. Importantly, a possible signature of Majorana fermions is the emergence of zero-bias conductance peaks in the transmission spectrum, which were reported in diverse systems during the past decade [17–21].

On the other hand, chiral molecules including double-stranded DNA (dsDNA) and single-helical protein have been receiving extensive attention. For instance, the spin selectivity effect was widely demonstrated in a variety of chiral molecules [22–27]. Topological states were reported in both dsDNA and single-helical molecules under a perpendicular electric field, and a Thouless quantum pump could be realized by rotating this electric field in the transverse plane [28,29].

Recently, the chiral molecule-superconductor hybrid systems attracted intensive interest. As early as 2001, Kasumov *et al.* firstly measured the electron transport through λ-DNA connected to superconducting electrodes in a magnetic field,

demonstrating a zero-bias conductance peak and proximity-induced superconductivity [30]. Then in 2016, Alpern *et al.* fabricated a hybrid system where single-helical protein of α-helical polyalanine self-assembled on a superconducting Nb film and observed a zero-bias conductance peak by using scanning tunneling spectroscopy [31]. They found that the peak height decreases with increasing the temperature and its width increases simultaneously, which may be related to unconventional triplet-pairing components with either *d*- or *p*-wave symmetry [31]. Recently, Millo *et al.* studied the electron transport properties of several chiral molecule-superconductor systems by adsorbing α-helical polyalanine on different conventional superconductors [32,33]. They observed a robust zero-bias conductance peak in the transmission spectrum, finding that the peak height is reduced by increasing the temperature and this peak vanishes in the strong magnetic field regime, which points toward the topological triplet *p*-wave superconductivity [32,33]. All these experiments share a common feature of zero-bias conductance peaks in the chiral molecule-superconductor systems and the underlying physics remains elusive. Theoretically, Tang *et al.* investigated the topological properties of a single-stranded DNA deposited on an *s*-wave superconductor, finding Majorana zero modes in this hybrid system [34]. Very recently, Chen *et al.* studied the transport properties of a dsDNA proximity-coupled by an *s*-wave superconductor, demonstrating Majorana zero modes as well as topological phase transitions in this dsDNA-superconductor system [35]. Notice that all these theoretical works focus on DNA molecules contacted by two normal-metal electrodes under homogeneous superconductivity, which are completely different from previous experiments [30–33].

In this paper, we perform a thorough theoretical study of the electronic properties of a single-helical protein, connected to a bottom superconducting electrode and a top normal-metal one, in the presence of a Zeeman field pointing toward the y axis, aiming to uncover the possible mechanism of the zero-bias conductance peaks observed in the experiments [31–33]. This two-terminal protein setup, as illustrated in Fig. 1, resembles the experiments that the α-helical polyalanine self-assembled normally on a conventional superconductor and the conductance was measured at the other end of the protein by an STM tip [31–33]. In the following, the bottom (top) electrode is termed as left (right) electrode as usual. In this protein-superconductor system, the pairing potential attenuates exponentially along the helix axis (z axis), which captures the main features of the experiments and is termed as decaying superconductivity here. We find that a zero-bias conductance peak of $2e^2/h$ is demonstrated at zero temperature and the peak height decreases with increasing the temperature, which is accompanied by the peak width broadening, and this zero-bias peak splits into two peaks by increasing the Zeeman field, consistent with the experiments [31–33]. Besides the existence of Majorana zero modes in a wide range of model parameters, a specific region is predicted in the case of decaying superconductivity, in which topologically nontrivial and trivial zero modes coexist and the bandgap remains unchanged. In particular, the topologically nontrivial zero modes can transform to the trivial ones in the absence of bandgap closing-reopening within this specific region, and
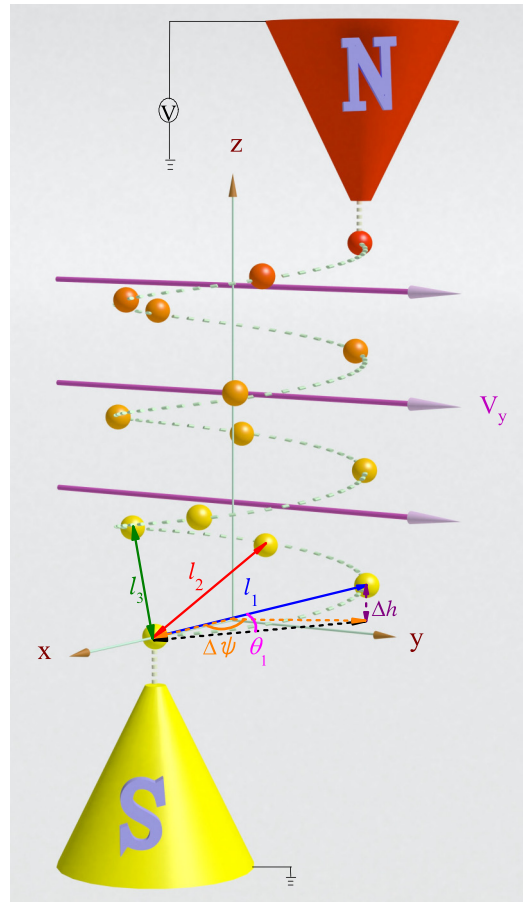

FIG. 1. Schematic diagram of a two-terminal single-helical protein, contacted by the bottom superconducting electrode S and the top normal-metal one N, in the presence of a perpendicular Zeeman field V_y, which points along the y axis. Here, each sphere represents an amino acid and the dashed line connecting these spheres depicts the helical structure of the protein. Because of the proximity-induced superconductivity by the superconducting electrode, the pairing potential emerges simultaneously in the protein and decays exponentially along the helix axis, as illustrated by the gradient color. $\Delta\psi$ and Δh are the twist angle and the stacking distance between the nearest-neighbor sites, respectively, $l_m = \sqrt{[2R\sin(m\Delta\psi/2)]^2 + (m\Delta h)^2}$ is the Euclidean distance between sites n and $n + m$, and $\theta_m = \arccos[2R\sin(m\Delta\psi/2)/l_m]$ is the space angle between the solid line l_m and the x − y plane, with R the radius. For clarity, the bottom electrode is named as left electrode and the top one as right electrode.

the critical pairing potential of the phase transition decreases exponentially with the superconducting decay exponent λ. Instead of localized at the ends, one of the two zero modes could be localized at any position of the single-helical protein and be shifted from the left end toward the right one by increasing the pairing potential. This decaying superconductivity and the associated phenomena, to the best of our knowledge, have not yet been reported in nanowire-superconductor systems.

The rest of the paper is organized as follows. In Sec. II, we introduce the Bogoliubov-de Gennes (BdG) Hamiltonian of the single-helical protein with superconductivity, and detail the methods of the nonequilibrium Green's function and

the scattering matrix. In Sec. III, the numerical results and discussion are displayed. Specifically, the differential conductance of the two-terminal protein is calculated by applying the nonequilibrium Green's function, the energy spectrum and the wave function are calculated by directly diagonalizing the BdG Hamiltonian without any coupling to the electrodes, and the Z_2 topological invariant is obtained from the scattering matrix method. In Sec. IV, a summary is given.

II. MODEL AND METHOD

We consider a single-helical protein connected to a superconducting electrode and a normal-metal one under a perpendicular magnetic field, as sketched in Fig. 1, which is similar to the experiments [31–33]. The total Hamiltonian of this two-terminal protein is written as

$$\mathcal{H} = \mathcal{H}_{\text{BdG}} + \mathcal{H}_{\text{L}} + \mathcal{H}_{\text{R}} + \mathcal{H}_{\text{c}}. \quad (1)$$

Here, $\mathcal{H}_{\text{BdG}}$ is the BdG Hamiltonian of the single-helical protein with superconductivity in the absence of any coupling to the electrodes. $\mathcal{H}_{\text{L}}$ and $\mathcal{H}_{\text{R}}$ are the Hamiltonians of the left superconducting electrode and the right normal-metal one, respectively, and $\mathcal{H}_{\text{c}}$ describes the coupling between the protein and the electrodes. $\mathcal{H}_{\text{BdG}}$ is expressed as

$$\mathcal{H}_{\text{BdG}} = \frac{1}{2} \sum_{n,n'} \Psi_n^\dagger \mathbf{H}_{\text{BdG}}(n, n') \Psi_{n'}, \quad (2)$$

with the matrix element

$$\mathbf{H}_{\text{BdG}}(n, n') = \begin{bmatrix} \mathcal{H}_{\text{p}}(n, n') + \mu\delta_{n,n'} & -i\Delta_n\hat{\sigma}_y\delta_{n,n'} \\ i\Delta_n^*\hat{\sigma}_y\delta_{n,n'} & -\mathcal{H}_{\text{p}}^*(n, n') - \mu\delta_{n,n'} \end{bmatrix}. \quad (3)$$

Here, $\Psi_n^\dagger = (c_{n\uparrow}^\dagger, c_{n\downarrow}^\dagger, c_{n\uparrow}, c_{n\downarrow})$, μ is the chemical potential, and $\delta_{n,n'}$ the Kronecker delta. Because of the proximity-induced superconductivity by the superconducting electrode, a pairing potential Δ_n emerges in the single-helical protein. Notice that since the superconducting wave function attenuates exponentially with the distance from the superconducting electrode, this pairing potential along the helix axis may be expressed as $\Delta_n = \Delta e^{-n/\lambda}$ [36–38]. Here, Δ is the pairing potential in the superconducting electrode, and λ is the decay exponent, which describes how fast the superconductivity attenuates along the protein. The unit of λ is the number of sites. $\mathcal{H}_{\text{p}}$ is the Hamiltonian of the protein without any superconductivity and reads [39]

$$\mathcal{H}_{\text{p}} = \sum_{n=1}^N \epsilon_n c_n^\dagger c_n + \sum_{n=1}^{N-1}\sum_{m=1}^{N-n} t_m c_n^\dagger c_{n+m} + \sum_{n=1}^N V_y c_n^\dagger \hat{\sigma}_y c_n$$
$$+ \sum_{n=1}^{N-1}\sum_{m=1}^{N-n} 2is_m \cos(\psi_{n,m}^-) c_n^\dagger \hat{\sigma}_{n,m} c_{n+m} + \text{H.c.}, \quad (4)$$

where $c_n^\dagger = (c_{n\uparrow}^\dagger, c_{n\downarrow}^\dagger)$ is the creation operator at site n of the protein with length N. ϵ_n is the on-site energy, $t_m = t_1 e^{-(l_m - l_1)/l_c}$ the mth neighboring hopping integral, V_y the Zeeman field strength, and $s_m = s_1 e^{-(l_m - l_1)/l_c}$ the renormalized spin-orbit coupling (SOC) [39]. Here, the Zeeman field is parallel to the positive y axis, and the

numerical results remain the same when it points along either the x axis or any selected orientation within the x-y plane. $l_m = \sqrt{[2R\sin(m\Delta\psi/2)]^2 + (m\Delta h)^2}$ is the Euclidean distance between sites n and $n + m$, l_c is the other decay exponent, which characterizes the long-range electron transport in the protein, R the radius, and $\Delta\psi$ (Δh) the twist angle (stacking distance) between the nearest-neighbor (NN) sites. $\hat{\sigma}_{n,m} = (\hat{\sigma}_x \sin\psi_{n,m}^+ - \hat{\sigma}_y \cos\psi_{n,m}^+)\sin\theta_m + \hat{\sigma}_z \cos\theta_m$, $\theta_m = \arccos[2R\sin(m\Delta\psi/2)/l_m]$, $\psi_{n,m}^\pm = (\psi_{n+m} \pm \psi_n)/2$, $\psi_n = n\Delta\psi$, and $\hat{\sigma}_{x,y,z}$ the Pauli matrices. Some of these structural parameters are shown in Fig. 1.

The Hamiltonians of the two electrodes and their coupling to the protein are written as

$$\mathcal{H}_{\text{L}} = \sum_k \epsilon_{k\text{L}} a_{k\text{L}}^\dagger a_{k\text{L}} + \sum_k (\Delta a_{k\uparrow\text{L}}^\dagger a_{-k\downarrow\text{L}}^\dagger + \Delta^* a_{-k\downarrow\text{L}} a_{k\uparrow\text{L}}), \quad (5)$$

$$\mathcal{H}_{\text{R}} = \sum_k \epsilon_{k\text{R}} a_{k\text{R}}^\dagger a_{k\text{R}}, \quad (6)$$

and

$$\mathcal{H}_{\text{c}} = \sum_k (V_k a_{k\text{L}}^\dagger c_1 + V_k a_{k\text{R}}^\dagger c_N + \text{H.c.}). \quad (7)$$

Here, $a_{k\alpha}^\dagger = (a_{k\uparrow\alpha}^\dagger, a_{k\downarrow\alpha}^\dagger)$ is the creation operator for an electron with wave vector k in the superconducting and normal-metal electrodes ($\alpha = \text{L, R}$), and V_k is the coupling between the protein and the electrodes. We emphasize that the left electrode is superconducting with the pairing potential Δ and the right one is normal metal. The retarded Green's function can be expressed as

$$\mathbf{G}^r(E) = [E\mathbf{I}_{4N} - \mathbf{H}_{\text{BdG}} - \mathbf{\Sigma}_{\text{L}}^r(E) - \mathbf{\Sigma}_{\text{R}}^r(E)]^{-1}, \quad (8)$$

where E is the electron energy, $\mathbf{I}_{4N}$ the identity matrix of size $4N$, and $\mathbf{\Sigma}_\alpha^r$ ($\alpha = \text{L, R}$) the retarded self-energy due to the coupling to electrode α. We consider the wide-band approximation and the retarded self-energy of the normal-metal electrode reads [23]

$$\Sigma_{\text{R}}^r(E) = -i\Gamma_{\text{R}}/2, \quad (9)$$

where $\Gamma_{\text{R}} = 2\pi \sum_k V_k^2 \delta(E - \epsilon_{k\text{R}})$ represents the coupling strength between the protein and the normal-metal electrode. While for the superconducting electrode, the retarded self-energy reads [40–43]

$$\mathbf{\Sigma}_{\text{L}}^r(E) = -i\Gamma_{\text{L}}\beta(E)\begin{pmatrix} 1 & \Delta/E \\ \Delta/E & 1 \end{pmatrix}, \quad (10)$$

where Γ_{L} is the protein-superconducting electrode coupling, and $\beta(E) = |E|/\sqrt{E^2 - \Delta^2}$ for $|E| > \Delta$ and $\beta(E) = E/i\sqrt{\Delta^2 - E^2}$ for $|E| < \Delta$. From the Keldysh formula, the lesser Green's function can be written as

$$\mathbf{G}^<(E) = [\mathbf{I} + \mathbf{G}^r(E)\mathbf{\Sigma}^r(E)]\mathbf{G}_0^<(E)[\mathbf{I} + \mathbf{\Sigma}^a(E)\mathbf{G}^a(E)]$$
$$+ \mathbf{G}^r(E)\mathbf{\Sigma}^<(E)\mathbf{G}^a(E)$$
$$= \mathbf{G}^r(E)[\mathbf{G}_0^r(E)]^{-1}\mathbf{G}_0^<(E)[\mathbf{G}_0^a(E)]^{-1}\mathbf{G}^a(E)$$
$$+ \mathbf{G}^r(E)\mathbf{\Sigma}^<(E)\mathbf{G}^a(E), \quad (11)$$

where $\mathbf{\Sigma}^<$ is the lesser self-energy, $\mathbf{G}^a = (\mathbf{G}^r)^\dagger$ the advanced Green's function, $\mathbf{\Sigma}^a = (\mathbf{\Sigma}^r)^\dagger$ the advanced self-energy, and

$\mathbf{G}_0^{r,a,<}$ the Green's functions of the isolated single-helical protein described by the BdG Hamiltonian in Eqs. (2) and (3). Since the term $[\mathbf{G}_0^r(E)]^{-1}\mathbf{G}_0^<(E)[\mathbf{G}_0^a(E)]^{-1}$ is zero for finite coupling between the protein and the normal-metal electrode, the first term on the right-hand side of Eq. (11) vanishes. The lesser Green's function can then be simplified as

$$\mathbf{G}^<(E) = \mathbf{G}^r(E)[\mathbf{\Sigma}_\mathrm{L}^<(E, V_\mathrm{b}) + \mathbf{\Sigma}_\mathrm{R}^<(E, V_\mathrm{b})]\mathbf{G}^a(E). \quad (12)$$

Here, $\mathbf{\Sigma}_\alpha^< = i\Gamma_\alpha \,\mathrm{diag}[f(E - \mu_\alpha), f(E - \mu_\alpha), f(E + \mu_\alpha), f(E + \mu_\alpha)]$ is the lesser self-energy due to the coupling to electrode α [44], V_b the bias voltage between the left and right electrodes, $f(E) = 1/[\exp(E/k_\mathrm{B}T) + 1]$ the Fermi-Dirac distribution function, k_B the Boltzmann constant, T the temperature, and $\mu_\mathrm{L} = 0$ and $\mu_\mathrm{R} = eV_\mathrm{b}$ the chemical potentials of the left and right electrodes, respectively. Then, the current flowing through the protein can be expressed as [44,45]

$$I_\mathrm{R} = \frac{e}{h} \int dE \,\mathrm{ReTr}\{\sigma[\mathbf{G}^<(E, V_\mathrm{b})\mathbf{\Sigma}_\mathrm{R}^a(E)$$
$$+ \mathbf{G}^r(E)\mathbf{\Sigma}_\mathrm{R}^<(E, V_\mathrm{b})]\}, \quad (13)$$

where $\sigma = \mathrm{diag}(1, 1, -1, -1 \cdots)$ accounts for different charges carried by electrons and holes. Finally, the differential conductance of the two-terminal protein can be evaluated as

$$G = \frac{dI_\mathrm{R}}{dV_\mathrm{b}}. \quad (14)$$

To elucidate the topological properties of this chiral molecule-superconductor system, the Z_2 topological invariant is evaluated. Since the protein with decaying superconductivity is aperiodic, we carry out the scattering matrix method instead of the one proposed by Kitaev [6], where the former can be applied to disordered systems [46]. This scattering matrix method has been widely used to characterize the topological properties of, e.g., disordered InAs wires [46] and inhomogeneous Rashba chains [47] coupled to a superconducting substrate, and can be described as follows. The scattering matrix links the incoming and outgoing wave amplitudes, and is defined as [46]

$$\begin{pmatrix} \mathbf{\Psi}_{+,\mathrm{R}} \\ \mathbf{\Psi}_{-,\mathrm{L}} \end{pmatrix} = \mathbf{S} \begin{pmatrix} \mathbf{\Psi}_{-,\mathrm{R}} \\ \mathbf{\Psi}_{+,\mathrm{L}} \end{pmatrix} = \begin{pmatrix} \mathbf{R} & \mathbf{T}' \\ \mathbf{T} & \mathbf{R}' \end{pmatrix} \begin{pmatrix} \mathbf{\Psi}_{-,\mathrm{R}} \\ \mathbf{\Psi}_{+,\mathrm{L}} \end{pmatrix}. \quad (15)$$

Here, $\mathbf{\Psi}_{+/-,\mathrm{L}}$ refers to the right/left-moving modes at the left end of the protein, $\mathbf{\Psi}_{+/-,\mathrm{R}}$ to the ones at the right end, and $\mathbf{S}$ is the scattering matrix. $\mathbf{R}$ ($\mathbf{R}'$) and $\mathbf{T}$ ($\mathbf{T}'$) are, respectively, the 4×4 reflection and transmission matrices at the right (left) end. On the other hand, this scattering matrix can alternatively be obtained from the Fisher-Li relation [47,48],

$$\mathbf{S} = \mathbf{I}_8 - 2\pi i \mathbf{W}^\dagger \mathbf{G}^r(E)\mathbf{W}, \quad (16)$$

where $\mathbf{I}_8$ is the 8×8 identity matrix. $\mathbf{W}$ represents the coupling between the protein and both electrodes, and is

TABLE I. Structural parameters of the single-helical protein.

Parameter	R	Δh	$\Delta\psi$	l_1	l_2	l_3
Value	0.25	0.15	$5\pi/9$	0.41	0.58	0.51

The distance (angle) is in unit nm (rad).

written as

$$\mathbf{W} = \begin{pmatrix} (\sqrt{\frac{\Gamma_\mathrm{R}}{2\pi}})\mathbf{I}_4 & \mathbf{0}_4 \\ \mathbf{0}_4 & \mathbf{0}_4 \\ \vdots & \vdots \\ \mathbf{0}_4 & \mathbf{0}_4 \\ \mathbf{0}_4 & (\sqrt{\frac{\Gamma_\mathrm{L}}{2\pi}})\mathbf{I}_4 \end{pmatrix}_{4N \times 8}, \quad (17)$$

where $\mathbf{0}_4$ is the 4×4 zero matrix. Then, the reflection and transmission matrices can be obtained from Eqs. (15)–(17). It has been reported that the reflection from one Majorana bound state generates a scattering phase π and leads to a phase factor of -1 [46]. As a result, the sign of $\det(\mathbf{R})$ equals the parity of the number m of Majorana bound states at each end of the protein, and the topological number Q is expressed as [47,49]

$$Q = \mathrm{sign}[\det(\mathbf{R})] = \mathrm{sign}[\det(\mathbf{R}')], \quad (18)$$

where $Q = 1(-1)$ corresponds to the topologically trivial (nontrivial) phase. Finally, the Z_2 topological invariant satisfies

$$(-1)^{Z_2} = Q. \quad (19)$$

It has been demonstrated analytically in Ref. [46] that the scattering matrix method is equivalent to the Kitaev method regarding the topological properties of periodic systems.

III. RESULTS AND DISCUSSION

For the single-helical protein, the on-site energy is taken as $\epsilon_n = 0$ to resemble a homogeneous protein of polyalanine used in the experiments, the NN hopping integral t_1 as the energy unit, and the renormalized SOC as $s_1 = 0.12t_1$. Then, the NN SOC of the protein is $s_1 \cos(\Delta\psi/2) \sim 0.077t_1$ and estimated to be 7.7 meV for $t_1 = 0.1$ eV, which is comparable with that reported in carbon nanotubes [50] but smaller than in 1D nanowires [43,51]. Although such small SOC normally weakens the superconducting gap, it could be enhanced by either decreasing the temperature or replacing the narrow-gap superconducting electrode with a wide-gap one. The structural parameters are set to $R = 0.25$ nm, $\Delta h = 0.15$ nm, $\Delta\psi = 5\pi/9$, and correspondingly the Euclidean distance between two NN sites is approximated as $l_1 \sim 0.41$ nm. The values of some basic structural parameters are listed in Table I, and all these parameters are chosen to mimic the α-helical protein and are the same as Ref. [39], which explains the spin-selective phenomenon observed in the α-helical protein [24]. The molecular length is fixed as 12.0 nm with $N = 80$, which is much shorter than that of 1D nanowires [43,51]. The chemical potential is chosen as $\mu = 1.7t_1$, the Zeeman field as $V_\mathrm{y} = 1.5t_1$, and the decay exponent characterizing the long-range electron transport in the protein is fixed as

$l_c = 0.09$ nm, which is close to the B-form DNA [52]. For the normal-metal electrode, the coupling strength is set to $\Gamma_R = 0.05t_1$ to account for poor protein-electrode contact [34]. While for the superconducting electrode, the pairing potential is taken as $\Delta = 0.8t_1$ and the coupling strength as $\Gamma_L = \Gamma_R$ for simplicity, because the differential conductance is obtained at the normal-metal electrode and does not depend on Γ_L. As the normal coherence length could range from tens of nanometers to hundreds of nanometers at low temperatures [53], the decay exponent simulating how the superconductivity attenuates along the protein is set to $\lambda = 100$. In this situation, the normal coherence length of the superconducting Nb film is about 15 nm for the protein, which is larger than the molecular length. For this short protein, our results demonstrate that topologically nontrivial modes can exist in a wide range of model parameters, which is different from other nanowire-superconductor systems where topologically nontrivial modes disappear for such short nanowires [43,51]. Besides, the topological properties of the protein-superconductor system remain unchanged for shorter protein with length being only 7.5 nm and different protein-electrode couplings. The values of all above-mentioned parameters will be used throughout the paper and all the calculations are performed at zero temperature, unless stated otherwise.

We first consider how the temperature T and the Zeeman field V_y affect the charge transport properties of the single-helical protein with decaying superconductivity, which will be termed as the protein-superconductor system for simplicity. Figure 2(a) shows the differential conductance G versus the bias voltage V_b by considering several values of T, which is obtained from Eq. (14). A zero-bias conductance peak of $2e^2/h$ is clearly demonstrated in the transmission spectrum at zero temperature [see the black-solid line in Fig. 2(a)], indicating the existence of two zero modes in the protein-superconductor system. When the temperature is increased from $T = 0$ K to 8 K, the peak height is progressively declined from $G = 2e^2/h$ to approximately $0.25e^2/h$, which is accompanied by the broadening of the peak width [see the other lines in Fig. 2(a)]. This conductance peak will finally vanish by further increasing T. These results are in good agreement with previous experiments that the peak height (width) decreases (broadens) with increasing T [31,33].

The above evolution phenomenon of the conductance peak with the temperature originates from the thermal broadening effect. We know that the electron distribution satisfies the Fermi-Dirac statistics, and all the electronic states of the electrode locating within the bias window $[-V_b/2, V_b/2]$ will contribute to the current I_R [see Eq. (13)] and thus to G. At zero temperature, the Fermi-Dirac distribution function is a step function and only the electronic states at the Fermi level of the electrode can affect G. Whereas at nonzero temperatures, the Fermi-Dirac distribution function has hyperbolic-tangent-like form and consequently the contribution of the electronic states at the Fermi level will be decreased. Instead, both electronic states below and above the Fermi level will influence G, giving rise to the thermal broadening effect. As a result, the peak height decreases with increasing T and consequently its width becomes wider. Since we consider an extremely small bias voltage between the left and right electrodes, only the electronic states of the protein-
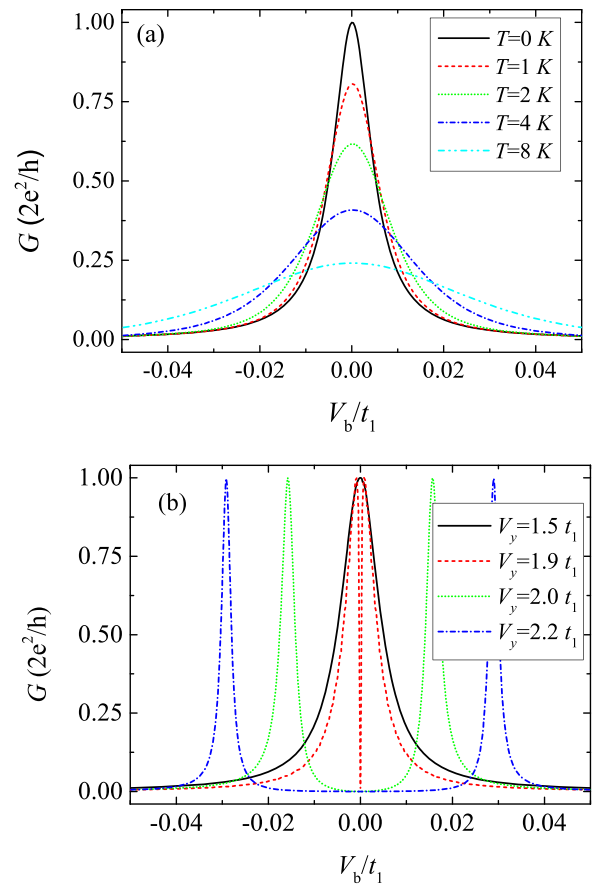

FIG. 2. Electron transport along a two-terminal single-helical protein by considering different temperatures T and Zeeman fields V_y. Differential conductance G vs bias voltage V_b for (a) various T with $V_y = 1.5t_1$ and for (b) several V_y at zero temperature. Here, the model parameters are $N = 80$, $\Delta = 0.8t_1$, $\mu = 1.7t_1$, and $\lambda = 100$. The temperature is compared by setting $t_1 = 0.1$ eV.

superconductor system around the Fermi level, i.e., the two zero modes [see the red- and green-solid lines in Fig. 3(a)], will attend the charge transport process. Therefore, the integral of G along the V_b axis remains unchanged for different temperatures [Fig. 2(a)].

We then study the effect of the Zeeman field, as shown in Fig. 2(b), which plots the bias voltage-dependent G at zero temperature for different V_y. It clearly appears that the conductance peak locates at zero-bias voltage for $V_y = 1.5t_1$ [see the black-solid line in Fig. 2(b)]. In contrast, this zero-bias conductance peak will disappear by increasing V_y and instead a pair of peaks emerge symmetrically with respect to the line $V_b = 0$ [see the other lines in Fig. 2(b)], which is attributed to the Majorana oscillation, as discussed below. These results are qualitatively consistent with the previous experiment that a zero-bias conductance peak appears for small magnetic field and splits into two peaks by increasing this magnetic field [33]. However, another experiment reported that the zero-bias conductance peak does not split with increasing the magnetic field upon adsorption of α-helical polyalanine on Au films grown on superconducting NbN [32], which may be related to strong hybridization effects at the chiral molecule-Au interface and deserve further investigations. Although the
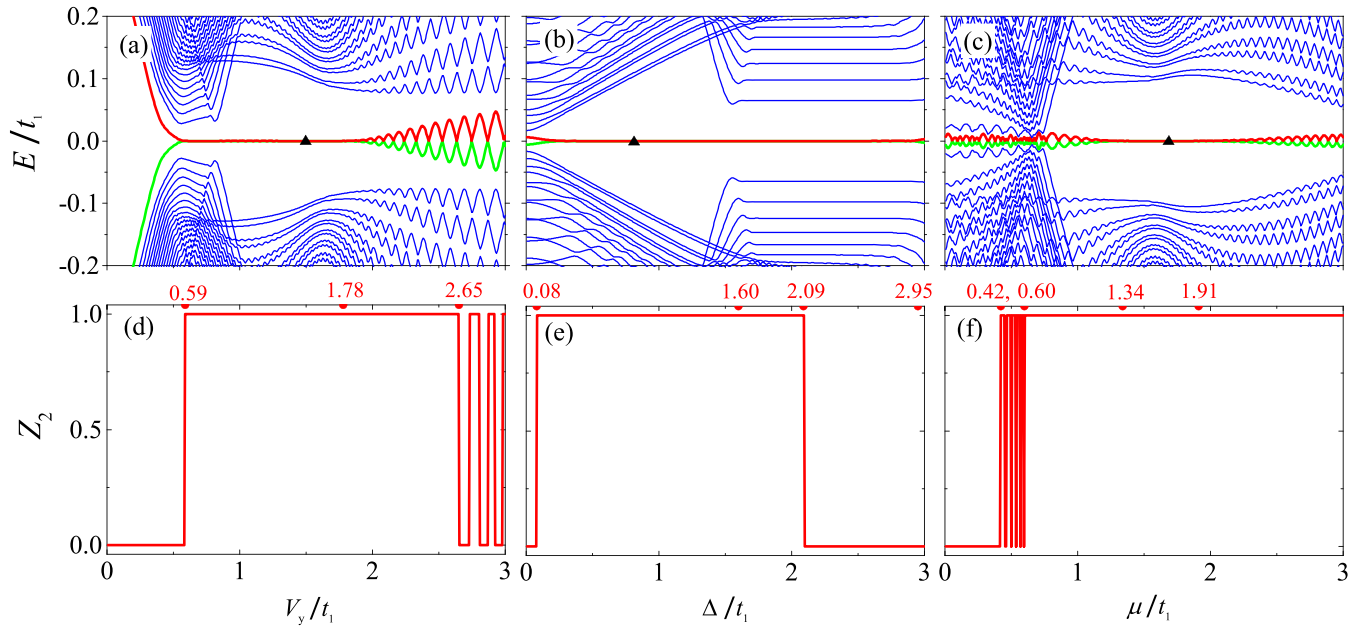
FIG. 3. Energy spectra and Z_2 topological invariants of the protein-superconductor system by changing the Zeeman field V_y, the pairing potential Δ, and the chemical potential μ. [(a)–(c)] Energy spectra as functions of V_y, Δ, and μ, respectively. [(d)–(f)] Z_2 invariants as functions of V_y, Δ, and μ, respectively. The triangles in (a)–(c) mark the point where the differential conductance in Fig. 2(a) is calculated.

zero-bias conductance peak suggests the existence of zero modes in the protein-superconductor hybrid system, its physical origin remains unclear.

To understand the physical nature of the zero-bias conductance peak and the possible topological properties of the protein-superconductor system, the energy spectrum and the Z_2 topological invariant are calculated by varying the Zeeman field V_y, the pairing potential Δ, and the chemical potential μ. Here, the energy spectrum and the wave function shown below are obtained by directly diagonalizing the BdG Hamiltonian in Eqs. (2) and (3), and the Z_2 topological invariant is calculated from the scattering matrix method in Eqs. (15)–(19). Figures 3(a) and 3(d) display the energy spectrum and the Z_2 topological invariant, respectively, as a function of V_y. One can see from Fig. 3(a) that the energy spectrum is always symmetric with respect to the line $E = 0$, owing to the intrinsic electron-hole symmetry of the BdG Hamiltonian [54,55]. In the small Zeeman field regime of $V_y < 0.59t_1$, a bandgap is clearly demonstrated due to the proximity-induced superconductivity and its width decreases almost linearly with increasing V_y [see the red- and green-solid lines in Fig. 3(a)]. This bandgap closes and reopens at $V_y \sim 0.59t_1$, implying a possible topological phase transition at this critical Zeeman field. This phase transition is further confirmed in Fig. 3(d) where the topological invariant changes from $Z_2 = 0$ to 1 at $V_y \sim 0.59t_1$. In the intermediate regime of $0.59t_1 < V_y < 1.78t_1$, the two modes closest to zero-energy overlap at $E = 0$ [see the red- and green-solid lines in Fig. 3(a)] and two Majorana zero modes with $Z_2 = 1$ appear in the energy spectrum [Fig. 3(d)], leading to the emergence of the zero-bias conductance peak [Fig. 2(a)]. While in the large Zeeman field regime of $V_y > 1.78t_1$, the two Majorana modes oscillate with increasing V_y and the oscillating amplitude increases almost linearly [see the right half part of Fig. 3(a)], which gives rise

to the splitting of the zero-bias conductance peak into two peaks [Fig. 2(b)]. This phenomenon is named as the Majorana oscillation [43,56] and regarded as a smoking gun for the existence of Majorana modes [51]. Indeed, the Majorana oscillation of small amplitude corresponds to the topologically nontrivial modes with $Z_2 = 1$. Interestingly, the oscillation of large amplitude refers to either the topologically nontrivial modes or the trivial ones, and the topological invariant oscillates between $Z_2 = 0$ and 1 for $V_y > 2.65t_1$ [see the rightmost part of Fig. 3(d)], which is termed as the Z_2 oscillation.

This Z_2 oscillation can be understood from the hybridization of the wave functions of the two modes closest to $E = 0$, which are generally localized at both ends of the protein. When the overlapping of the wave functions at the left and right ends is negligible, these two modes are Majorana zero modes with $Z_2 = 1$. When the wave function overlapping is gradually enhanced, this hybridization leads to the deviation of Majorana modes from $E = 0$ [51]. The stronger the hybridization is, the larger the deviation of the two modes from zero energy. Subsequently, the Majorana oscillation takes place and the oscillating amplitude increases almost linearly with V_y, see the region of $V_y > 1.78t_1$ in Fig. 3(a). Provided this hybridization is so weak that the wave functions at the two ends can be well separated from each other, the two modes are still topologically nontrivial with $Z_2 = 1$, see the region of $1.78t_1 < V_y < 2.65t_1$ in Fig. 3(d). When the hybridization becomes sufficiently strong that the wave functions cannot be well separated from each other, the topological invariant oscillates between $Z_2 = 0$ and 1, see the region of $V_y > 2.65t_1$ in Fig. 3(d), which is similar to the Majorana oscillation. In this situation, the two modes transform frequently between the topologically nontrivial and trivial modes with increasing V_y, leading to possible multiple topological phase transitions in the large Zeeman field regime. In case that the protein is
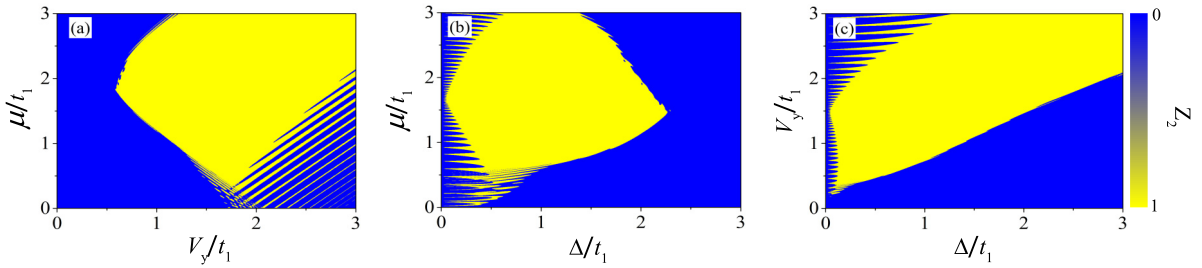
FIG. 4. Phase diagrams of the protein-superconductor system in the parameter space of the Zeeman field V_y, the pairing potential Δ, and the chemical potential μ. (a) Z_2 topological invariant vs V_y and μ. (b) Z_2 vs Δ and μ. (c) Z_2 vs Δ and V_y. The remaining parameters are the same as those in Fig. 2.

longer than the normal coherence length, the region of the Z_2 oscillation shrinks with increasing λ and finally disappears when the hybridization of the wave functions at the two ends becomes negligible.

We then investigate the effect of the superconducting pairing potential Δ on the energy spectrum and the topological invariant, as presented in Figs. 3(b) and 3(e), respectively. It is clear that there does not exist a bandgap in the absence of pairing potential, and the two modes closest to $E = 0$ seem to be separated from each other at $\Delta = 0$ [see the red- and green-solid lines in Fig. 3(b)], owing to finite-size effects. When the pairing potential is incorporated, a bandgap appears and its width presents nonmonotonic dependence on Δ. This gap width firstly increases with Δ and then decreases with Δ [see the left part of Fig. 3(b)]. Interestingly, this bandgap remains unchanged for $1.60t_1 < \Delta < 2.95t_1$ [see the right half part of Fig. 3(b)], of which this range is named as specific region. We stress that several important phenomena can be identified in this specific region, as further discussed below. In addition, the two modes quickly overlap at $E = 0$ with increasing Δ and two zero modes appear in a very wide range of Δ, which can be divided into two types as characterized by the topological invariant. The topological invariant changes from $Z_2 = 0$ for $\Delta < 0.08t_1$ to $Z_2 = 1$ for $0.08t_1 < \Delta < 2.09t_1$, and back to $Z_2 = 0$ for $\Delta > 2.09t_1$ [Fig. 3(e)], implying a topological phase transition at the critical values of $\Delta \sim 0.08t_1$ and $2.09t_1$. It is interesting that beyond the Majorana zero modes for $\Delta < 2.09t_1$, topologically trivial zero modes also exist in the protein-superconductor system for $\Delta > 2.09t_1$. We point out that these topologically trivial zero modes can generate zero-bias conductance peaks in the transmission spectrum as well, just as the Majorana zero modes. Further inspection demonstrates that the Majorana zero modes can be distinguished from the topologically trivial ones by on-site energy disorder generated by, e.g., stochastic population of external atoms and counterions around the protein, where the former remains in the strong disorder regime and the latter becomes fragile in the presence of disorder. Additionally, the Majorana zero modes can be discerned from Andreev bound states by, e.g., introducing a sharp local potential in a nanowire [57], probing the correlation between differential conductance spectra measured at the two ends of a nanowire [58], and implementing a strongly dissipative electrode [59].

Figures 3(c) and 3(f) show the energy spectrum and the topological invariant, respectively, as a function of μ. One clearly identifies the oscillation phenomenon that the two modes closest to $E = 0$ oscillate sharply with increasing μ for $\mu < 1.34t_1$, and the oscillation pattern is significantly modified across the critical value of $\mu \sim 0.74t_1$ at which a bandgap takes place [see the red- and green-solid lines in Fig. 3(c)]. In the low chemical potential regime of $\mu < 0.42t_1$, although the oscillating amplitude is small, the topological invariant is $Z_2 = 0$ [Fig. 3(f)] and consequently the two modes are topologically trivial. For $0.42t_1 < \mu < 0.60t_1$, the topological invariant oscillates dramatically between $Z_2 = 0$ and 1, which originates from the hybridization effect between the wave functions of the two modes closest to $E = 0$ as discussed above. While for $0.60t_1 < \mu < 1.34t_1$, the topological invariant becomes $Z_2 = 1$ and the two modes are topologically nontrivial. By further increasing μ, the two modes become degenerated at $E = 0$ with $Z_2 = 1$ and the Majorana zero modes emerge for $1.34t_1 < \mu < 1.91t_1$. In the high chemical potential regime of $\mu > 1.91t_1$, the two modes oscillate around $E = 0$ again and the Majorana oscillation is identified with $Z_2 = 1$, where the topologically nontrivial zero and nonzero modes coexist.

We then investigate the topological phase diagrams of the protein-superconductor system in different parameter spaces by taking into account V_y, Δ, and μ. Figure 4(a) shows the topological invariant as functions of V_y and μ. One can see that the topological invariant is $Z_2 = 0$ in the small Zeeman field regime of $V_y < 0.58t_1$ [see the leftmost blue part in Fig. 4(a)] and thus all the modes are topologically trivial, which is independent of μ. When the Zeeman field is increased up to $V_y \sim 0.58t_1$, the topological invariant could transform to $Z_2 = 1$ and gives rise to the Majorana modes. This is consistent with the previous study that a sufficiently large Zeeman field is necessary to drive effective p-wave superconducting states into topological superconducting phase [60], where the p-wave superconductivity in the single-helical protein could be induced by the combination of SOC and pairing potential [61]. With increasing V_y, the range of μ supporting the Majorana modes with $Z_2 = 1$ is enlarged almost linearly [see the yellow part in Fig. 4(a)], which is accompanied by the topological phase transition at the blue-yellow border. Remarkably, a number of yellow strips are found in a wide area of the $V_y - \mu$ space [see the bottom-right part in Fig. 4(a)], because of the Majorana oscillation. It is clear that the topological invariant oscillates between $Z_2 = 0$ and 1 by increasing either V_y or μ, implying multiple topological phase transitions.

Figures 4(b) and 4(c) plot the topological invariant in the $\Delta - \mu$ space and the $\Delta - V_y$ space, respectively. It can be
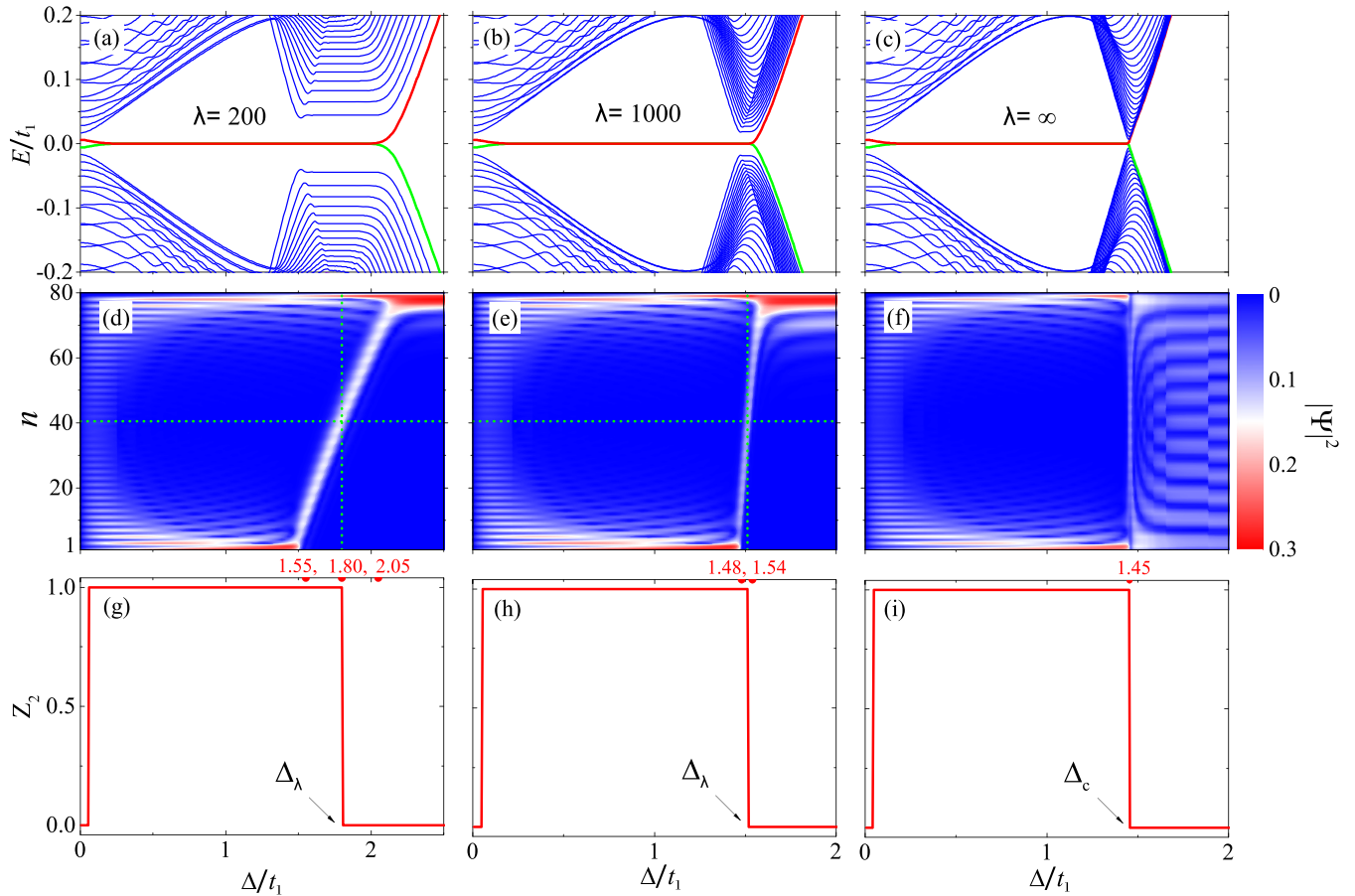
FIG. 5. Energy spectra, wave functions, and Z_2 topological invariants of the protein-superconductor system by considering both decaying and homogeneous superconductivity, as a function of the pairing potential Δ. [(a)–(c)] Energy spectra vs Δ for $\lambda = 200$, 1000, and ∞, respectively. [(d)–(f)] Spatial distribution of wave functions $|\Psi|^2$ of the zero modes for $\lambda = 200$, 1000, and ∞, respectively, as a function of Δ. [(g)–(i)] Corresponding Z_2 invariants vs Δ. Here, the vertical and horizontal cyan-dotted lines in (d) and (e) denote the lines $\Delta = \Delta_\lambda$ and $n = (N+1)/2$, respectively. Δ_λ corresponds to the topological phase transition point in the case of decaying superconductivity, and Δ_c to the homogeneous one. The other parameters are the same as those in Fig. 2.

seen that all the modes are topologically trivial for extremely weak pairing potentials of $\Delta < 0.02t_1$, irrespective of μ and V_y. This critical value of $\Delta \sim 0.02t_1$ decreases with increasing N and remains nonzero in the limit $N \to \infty$, so do the other ones, e.g., $\Delta \sim 0.08t_1$ in Fig. 3(e). In other words, a finite pairing potential is necessary to ensure topologically nontrivial phases. When the pairing potential reaches $\Delta \sim 0.02t_1$, a number of discrete Majorana modes are identified in both the $\Delta - \mu$ space and the $\Delta - V_y$ space. And the Majorana oscillation emerges simultaneously, where the topological invariant oscillates with increasing μ or V_y albeit of no oscillation phenomenon by changing Δ. In the $\Delta - \mu$ space, the chemical potential range of the Majorana modes decreases with Δ and all the modes return to the topologically trivial ones when $\Delta > 2.30t_1$, which is accompanied by the disappearance of the Majorana oscillation in the strong pairing potential regime of $\Delta > 1.08t_1$, as shown in Fig. 4(b). Contrarily, both the Majorana oscillation and the Majorana modes remain in a wide range of Δ in the $\Delta - V_y$ space [Fig. 4(c)]. Additionally, the Majorana modes could exist at extremely low even zero chemical potential [Figs. 4(a) and 4(b)] and at small Zeeman fields of $V_y \sim 0.18t_1$ [Fig. 4(c)]. Therefore, we conclude

that the Majorana modes can be observed in the protein-superconductor system in a very wide range of the Zeeman field, the pairing potential, and the chemical potential. We stress that the phase diagrams of the protein-superconductor system, such as the oscillation of the topological invariant, are different from previous studies on single-stranded DNA [34], dsDNA [35], multichannel Majorana nanowires [62], and antiferromagnetic chains [63], which originate from the decaying superconductivity and finite-size effects.

We have demonstrated above the topologically nontrivial zero modes as well as the trivial ones in the single-helical protein contacted by the left superconducting electrode and the right normal-metal electrode. Nevertheless, the physical origin of these trivial zero modes and the influence of the decaying superconductivity remain unclear. In the following, we investigate the topological properties of the protein-superconductor system by taking into account several decay exponents λ.

Figures 5(a) and 5(b) show the energy spectrum versus Δ with the decay exponent $\lambda = 200$ and 1000, respectively. As a comparison, Fig. 5(c) displays the energy spectrum by considering homogeneous superconductivity along the

single-helical protein, i.e., $\lambda = \infty$. The energy spectra are similar for different values of λ, including the evolution of the bandgap and the two modes closest to zero energy, as shown in Figs. 3(b) and 5(a)–5(c). Interestingly, there always exists a specific region in the protein-superconductor system with decaying superconductivity, where the gap width remains constant by changing Δ. The range of this specific region shrinks from $[1.60t_1, 2.95t_1]$ for $\lambda = 100$ to $[1.55t_1, 2.05t_1]$ for $\lambda = 200$, and to $[1.48t_1, 1.54t_1]$ for $\lambda = 1000$, and the associated bandgap decreases with increasing λ. In sharp contrast, this specific region vanishes in the case of homogeneous superconductivity and is reduced to a single point at which the bandgap closes and reopens [Fig. 5(c)]. Since the bandgap closing-reopening process refers to a topological phase transition [64], intriguing phenomena may be expected in this specific region, as shown below. Besides, the two zero modes will be separated from each other at sufficiently strong pairing potential and finally the bandgap increases with Δ.

Figures 5(d)–5(f) show the spatial distribution of wave function $|\Psi|^2$ of the zero modes versus Δ with $\lambda = 200$, 1000, and ∞, respectively, while Figs. 5(g)–5(i) plot the corresponding topological invariants. At extremely weak pairing potential regime of $\Delta < 0.05t_1$, the wave function could be delocalized over the whole system for both decaying and homogeneous superconductivity [see the leftmost parts of Figs. 5(d)–5(f)], and the associated topological invariant is $Z_2 = 0$, owing to finite-size effects and weak proximity-induced superconductivity. We point out that the wave function will be localized at the two ends of the protein for long molecular length. With increasing Δ, the Majorana zero modes with $Z_2 = 1$ appear and the wave function is localized at the two ends as expected, for whatever the values of λ. It is surprising that in the case of decaying superconductivity, the localized wave function can gradually move from the left end contacted by the superconducting electrode to the right end with increasing Δ when the pairing potential surpasses the critical value [see the white-oblique trajectories in Figs. 5(d) and 5(e)]. In other words, the wave function can be localized at any position of the protein by properly tuning Δ. Here, the moving of the localized wave function is termed as the migration process, which only occurs in the aforementioned specific region of the protein-superconductor system with decaying superconductivity. This migration process would be beneficial for implementing the braiding of the Majorana zero modes and for constructing the topological qubits [65,66].

Besides the tunable position of the localized wave function, we then discuss the other interesting phenomena in this specific region. It is well known that the topological phase transition is usually accompanied by the bandgap closing-reopening [64], as further confirmed in Figs. 5(c) and 5(i) where the bandgap closes and reopens at $\Delta_c \sim 1.45t_1$ with the topological invariant changing from $Z_2 = 1$ to 0. Surprisingly, this picture is completely modified by considering the decaying superconductivity. During the migration process in which the bandgap remains constant, the topological invariant can transform from $Z_2 = 1$ to 0 at the critical value Δ_λ, indicating a topological phase transition at Δ_λ. This critical pairing potential decreases from $\Delta_\lambda \sim 2.09t_1$ for $\lambda = 100$ to $\Delta_\lambda \sim 1.80t_1$ for $\lambda = 200$, and to $\Delta_\lambda \sim 1.51t_1$ for $\lambda = 1000$. Interestingly, the dependence of Δ_λ on λ can be

approximated as

$$\Delta_\lambda \sim \Delta_c e^{(N+1)/2\lambda}. \tag{20}$$

Furthermore, we find that the crossing point between the lines $\Delta = \Delta_\lambda$ and $n = (N+1)/2$ locates in the middle of the white-oblique trajectories [see the cyan-dotted lines in Figs. 5(d) and 5(e)]. This indicates that for the Majorana zero modes, the wave function is localized at the left half part and the right end of the protein; whereas for the topologically trivial zero modes, it is localized at the right half part and the right end. As a result, the topologically nontrivial and trivial zero modes can be discerned experimentally by measuring their local density of states, i.e., $\rho(n) = |\Psi(n)|^2$. By further increasing Δ, the wave function is localized at the right end for the decaying superconductivity [see the rightmost parts of Figs. 5(d) and 5(e)], in sharp contrast to the homogenous case that the wave function will be delocalized over the whole system [see the rightmost part of Fig. 5(f)].

Although we have demonstrated the topologically nontrivial and trivial zero modes in the single-helical protein when the superconductivity decays exponentially along the helix axis, three issues remain unclear: (i) the emergence of the specific region with constant bandgap in the case of decaying superconductivity, (ii) the occurrence of the migration process and the topological phase transition in this specific region, and (iii) the reason why the phase transition point decreases with increasing the decay exponent. We will attempt to solve these issues in the following.

The emergence of the specific region with constant bandgap may be understood from the bandgap evolution in both periodic and aperiodic systems, as shown in Fig. 6. For the periodic protein with homogeneous superconductivity, the bandgap satisfies $E_g = 0$ at $\Delta = \Delta_c$ and increases almost linearly when the pairing potential deviates from Δ_c [Figs. 5(c) and 6(a)], i.e., $E_g \sim \beta|\Delta - \Delta_c|$ with β the slope. The phase is topologically nontrivial for $\Delta < \Delta_c$ and becomes trivial for $\Delta > \Delta_c$. In the case of decaying superconductivity, i.e., $\Delta_n = \Delta e^{-n/\lambda}$, this aperiodic protein can be divided into many slices and the pairing potential could be constant within each slice when it is sufficiently short. Here, each slice is taken as a single site. Then, the nth site of Δ_n refers to a sub-bandgap $E'_g(n) \sim \beta|\Delta e^{-n/\lambda} - \Delta_c|$, just the same as the periodic protein. For large λ, the pairing potential along the helix axis decreases almost linearly [Fig. 6(b)] and thus the sub-bandgap at site n can be simplified as $E'_g(n) \sim \beta \Delta_c |\frac{n-n_c}{\lambda}|$ with $n_c \equiv \lambda \ln(\Delta/\Delta_c)$. Subsequently, a "V"-shaped potential, generated from these site-dependent sub-bandgaps, emerges in the aperiodic protein with decaying superconductivity for a specific Δ [Fig. 6(c)], where the left (right) edge of this "V" shape corresponds to $\Delta_n > \Delta_c$ ($\Delta_n < \Delta_c$). This "V"-shaped potential confines the charge transport through the aperiodic protein, leading to discrete energy levels and the appearance of a bandgap E_g in the energy spectrum. In the vicinity of Δ_c, the "V"-shaped potential $E'_g(n) \sim \beta \Delta_c |\frac{n-n_c}{\lambda}|$ remains unchanged for different Δ and this "V" shape moves parallel toward the right end of the protein with increasing Δ [Figs. 6(b) and 6(c)]. This implies that the discrete energy levels induced by the "V"-shaped potential remain the same for different Δ, leading to the specific region of constant bandgap in the aperiodic
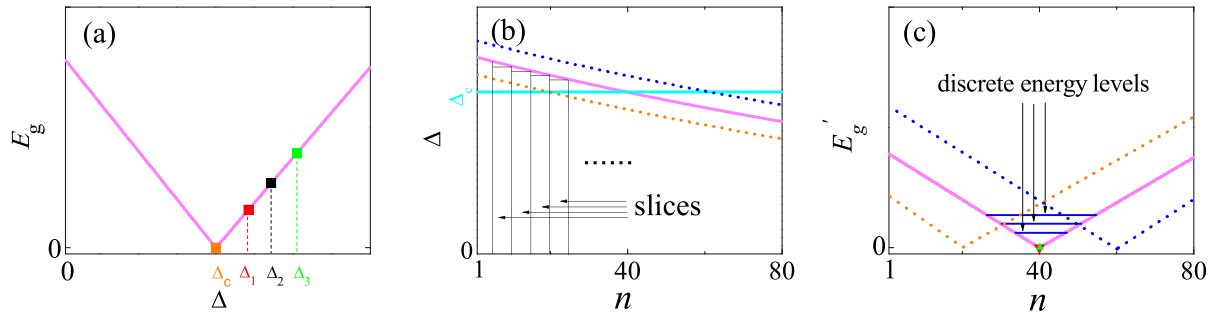
FIG. 6. Schematics of discrete energy levels and specific region of constant bandgap in the aperiodic protein with decaying superconductivity. (a) Dependence of bandgap E_g on the pairing potential Δ for the periodic protein with homogeneous superconductivity. (b) Decaying pairing potential along the helix axis of the aperiodic protein with decaying superconductivity, which can be divided into many slices of constant pairing potential. (c) "V"-shaped confinement produced by site-dependent sub-bandgaps $E'_g(n)$ in the aperiodic protein with decaying superconductivity. Here, the seemingly linear dependence of Δ_n on n in the aperiodic protein originates from the fact that the decay exponent of $\lambda = 100$ is larger than the molecular length of $N = 80$. Δ_c refers to the critical pairing potential at which the topological phase transition occurs in the periodic protein with homogeneous superconductivity.

protein with decaying superconductivity. Furthermore, when the decay exponent λ is gradually increased, the "V" shape becomes flatter and the induced confinement will be reduced, leading to the decrement of the bandgap [Figs. 3(b), 5(a), and 5(b)]. In the limit of $\lambda \to \infty$, the "V" shape becomes completely flat accompanied with the disappearance of the confinement, and thus the bandgap vanishes [Fig. 5(c)]. Therefore, the aperiodic protein possesses a specific region of constant bandgap and the periodic protein with homogeneous superconductivity can be regarded as a special case of the aperiodic protein in the limit of $\lambda \to \infty$.

We then interpret the interesting phenomena in this specific region. Figures 7(a)–7(d) show the schematic diagrams of the relation between the topological phase and the pairing potential in the protein-superconductor system, where the first panel corresponds to the homogeneous superconductivity and the remaining ones to the decaying superconductivity. Here, the black-solid lines describe the evolution of the pairing potential along the single-helical protein and the green-solid ones show the wave function $|\Psi|^2$. All the orange- and cyan-dotted lines denote the critical pairing potential Δ_c for the homogeneous superconductivity, where the topological phase transition occurs. The yellow regions refer to the topologically nontrivial phase and the red ones to the trivial phase. For the homogeneous superconductivity, i.e., $\Delta_n = \Delta$, the Majorana zero modes appear when $\Delta_n < \Delta_c$, as characterized by the yellow region in Fig. 7(a). Correspondingly, the zero modes are localized at both ends of the protein and the wave function is symmetric with respect to the line $n = (N+1)/2$ [see the black-solid line in Fig. 7(a)]. When $\Delta_n > \Delta_c$, a topological phase transition takes place and all the modes become topologically trivial, which will be characterized by the red region (not shown here).

We then consider the pairing potential decays exponentially along the protein, i.e., $\Delta_n = \Delta e^{-n/\lambda}$. In the limit case $\Delta_1 < \Delta_c$ where all the pairing potentials in the protein are smaller than Δ_c, the Majorana zero modes will emerge [see the yellow region in Fig. 7(b)] and be localized at both ends as well albeit of asymmetric wave function [see the green-solid line in Fig. 7(b)]. In the other limit case $\Delta_N > \Delta_c$ that all the pairing potentials are larger than Δ_c, the Majorana zero

modes transform to the topologically trivial ones and will be localized at the right end [see the red region and the green-solid line in Fig. 7(d)].

Of particular interest is the intermediate regime where $\Delta_N < \Delta_c < \Delta_1$, which is just the aforementioned specific region in the protein-superconductor system and will be discussed in detail as follows. As shown above, the aperiodic protein with decaying superconductivity could be divided into two segments by the criterion Δ_c at the specific site N' where
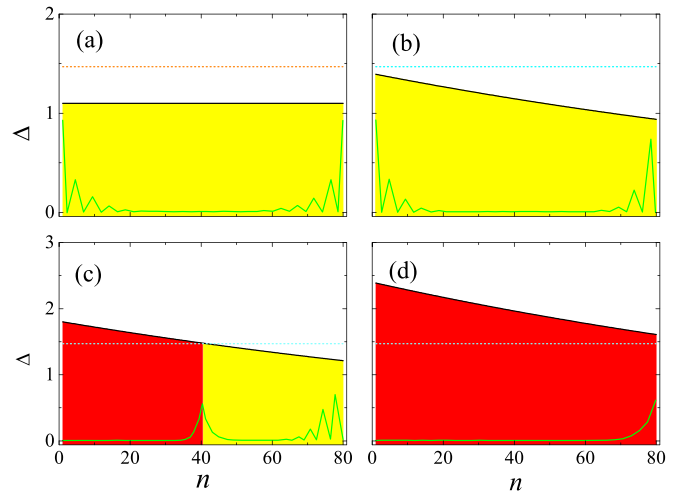

FIG. 7. Schematics of the topological properties and the spatial distribution of wave function $|\Psi|^2$ in the protein-superconductor system by considering both decaying and homogeneous superconductivity. (a) Homogeneous superconductivity with all the pairing potentials $\Delta_n = \Delta$ and $\Delta < \Delta_c$. Decaying superconductivity with the pairing potential satisfying (b) $\Delta_1 < \Delta_c$, (c) $\Delta_N < \Delta_c < \Delta_1$, and (d) $\Delta_N > \Delta_c$. Notice that the pairing potential along the helix axis attenuates exponentially and thus $\Delta_N < \Delta_{N-1} < \cdots < \Delta_1$. Here, the black-solid lines describe Δ_n at site n of the single-helical protein and the green-solid ones show $|\Psi|^2$. The orange- and cyan-dotted lines denote the critical pairing potential Δ_c for the homogeneous superconductivity, at which the topological phase transition takes place. The yellow regions refer to the topologically nontrivial phase and the red ones to the trivial phase.

$\Delta_{N'+1} < \Delta_c < \Delta_{N'}$. In the left segment, all the pairing potentials satisfy $\Delta_n > \Delta_c$ and this segment is topologically trivial regarding the criterion Δ_c [see the red region in Fig. 7(c)]. Contrarily, all the pairing potentials in the right segment satisfy $\Delta_n < \Delta_c$, which is topologically nontrivial and identified by the yellow region in Fig. 7(c), just the same as Fig. 7(b). As a result, one zero mode will always be localized around the site N', i.e., the topologically nontrivial-trivial interface [see the green-solid line in Fig. 7(c)]. With increasing Δ, the crossing between the black-solid line and the cyan-dotted one moves toward the right end, and thus the zero mode will be shifted from the left end to the right end, as can be seen from the white-oblique trajectories in Figs. 5(d) and 5(e). Although this zero mode can be localized at any site of the protein in this specific region, the topological properties of the whole aperiodic protein are determined by the interplay between the topologically nontrivial segment and the trivial one, which may be simply judged by the segment length. In other words, when the topologically nontrivial segment is longer than the trivial one, the former segment dominates the electronic properties of the protein and thus the topological invariant characterizing the topological properties of the whole systems is $Z_2 = 1$. Contrarily, when the topologically nontrivial segment is shorter than the trivial one, the latter segment becomes dominant and the topological invariant switches to $Z_2 = 0$. As a result, the topological invariant changes from $Z_2 = 1$ to 0 when the left mode passes through the middle of the protein. Therefore, the critical pairing potential Δ_λ of the topological phase transition for the decaying superconductivity is expressed as $\Delta_{(N+1)/2} = \Delta_\lambda e^{-(N+1)/2\lambda} = \Delta_c$, which is just Eq. (20) derived from the numerical calculations.

IV. CONCLUSIONS

In summary, we investigate theoretically the topological properties of a single-helical protein sandwiched between a superconducting electrode and a normal-metal one. In this protein-superconductor system, we firstly address the decaying superconductivity that the pairing potential attenuates exponentially along the helix axis of the protein, which is closely related to previous experiments. Our numerical results are qualitatively consistent with these experiments that a zero-bias conductance peak of conductance quantum is observed at zero temperature and the peak height (width) decreases (broadens) with increasing the temperature, and this zero-bias peak splits into two peaks by increasing the Zeeman field. Besides, this protein-superconductor system exhibits Majorana zero modes in a wide range of model parameters. In

sharp contrast to homogeneous superconductivity, a specific region is demonstrated in the protein-superconductor system with decaying superconductivity, where the bandgap remains constant. In particular, both topologically nontrivial and trivial zero modes exist in this specific region, and the topologically nontrivial zero modes can transform to the trivial ones in the absence of bandgap closing-reopening. For the Majorana zero modes, the wave function is localized at the left half part and the right end of the single-helical protein; whereas for the topologically trivial zero modes, it is localized at the right half part and the right end, which may provide an experimentally accessible way to discern the topologically nontrivial and trivial zero modes in the protein-superconductor system. In other words, instead of localized at the ends, one of the two zero modes could be localized at any position of the protein and be shifted from the left end toward the right one by increasing the pairing potential. Our theoretical study offers a unique perspective for the emergence of zero-bias conductance peaks in previous experiments and a deep understanding of the intriguing topological properties of chiral molecule-superconductor systems. The single-helical protein may provide an appealing platform to study Majorana physics, because Majorana modes can exist in the protein but disappear in one-dimensional nanowires with such small spin-orbit coupling and short system size.

Finally, we would like to point out that this decaying superconductivity and the associated interesting phenomena have not yet been reported in previous studies. These phenomena induced by the decaying superconductivity, such as the coexistence of topologically nontrivial and trivial zero modes, as well as the topological phase transition without bandgap closing-reopening, may also exist in inorganic nanowire-superconductor systems. This avenue deserves further investigation and our paper may stimulate the interest on chiral molecule-superconductor systems.

[1] E. Majorana, Teoria simmetrica dell′elettrone e del positrone, Nuovo. Cim. **14**, 171 (1937).

[2] N. Read and D. Green, Paired states of fermions in two dimensions with breaking of parity and time-reversal symmetries and the fractional quantum Hall effect, Phys. Rev. B **61**, 10267 (2000).

[3] R. Jackiw and P. Rossi, Zero modes of the vortex-fermion system, Nucl. Phys. B **190**, 681 (1981).

[4] D. A. Ivanov, Non-Abelian Statistics of Half-Quantum Vortices in *p*-Wave Superconductors, Phys. Rev. Lett. **86**, 268 (2001).

[5] L. Fu and C. L. Kane, Superconducting Proximity Effect and Majorana Fermions at the Surface of a Topological Insulator, Phys. Rev. Lett. **100**, 096407 (2008).

[6] A. Y. Kitaev, Unpaired Majorana fermions in quantum wires, Phys. Usp. **44**, 131 (2001).

[7] L. Jiang, T. Kitagawa, J. Alicea, A. R. Akhmerov, D. Pekker, G. Refael, J. I. Cirac, E. Demler, M. D. Lukin, and P. Zoller, Majorana Fermions in Equilibrium and in Driven Cold-Atom Quantum Wires, Phys. Rev. Lett. **106**, 220402 (2011).

[8] I. C. Fulga, A. Haim, A. R. Akhmerov, and Y. Oreg, Adaptive tuning of Majorana fermions in a quantum dot chain, New J. Phys. **15**, 045020 (2013).

[9] S. Nadj-Perge, I. K. Drozdov, B. A. Bernevig, and A. Yazdani, Proposal for realizing Majorana fermions in chains of magnetic atoms on a superconductor, Phys. Rev. B **88**, 020407(R) (2013).

[10] A. Yazdani, B. A. Jones, C. P. Lutz, M. F. Crommie, and D. M. Eigler, Probing the local effects of magnetic impurities on superconductivity, Science **275**, 1767 (1997).

[11] K. Pöyhönen, A. Weststrom, J. Röntynen, and T. Ojanen, Majorana states in helical Shiba chains and ladders, Phys. Rev. B **89**, 115109 (2014).

[12] S. Nadj-Perge, I. K. Drozdov, J. Li, H. Chen, S. Jeon, J. Seo, A. H. MacDonald, B. A. Bernevig, and A. Yazdani, Observation of Majorana fermions in ferromagnetic atomic chains on a superconductor, Science **346**, 602 (2014).

[13] J. Li, H. Chen, I. K. Drozdov, A. Yazdani, B. A. Bernevig, and A. H. MacDonald, Topological superconductivity induced by ferromagnetic metal chains, Phys. Rev. B **90**, 235433 (2014).

[14] M. Ruby, F. Pientka, Y. Peng, F. von Oppen, B. W. Heinrich, and K. J. Franke, End States and Subgap Structure in Proximity-Coupled Chains of Magnetic Adatoms, Phys. Rev. Lett. **115**, 197204 (2015).

[15] S. Jeon, Y. Xie, J. Li, Z. Wang, B. A. Bernevig, and A. Yazdani, Distinguishing a Majorana zero mode using spin resolved measurements, Science **358**, 772 (2017).

[16] H. Kim, A. Palacio-Morales, T. Posske, L. Rózsa, K. Palotás, L. Szunyogh, M. Thorwart, and R. Wiesendanger, Toward tailoring Majorana bound states in artificially constructed magnetic atom chains on elemental superconductors, Sci. Adv. **4**, eaar5251 (2018).

[17] J. D. Sau, R. M. Lutchyn, S. Tewari, and S. Das Sarma, Generic New Platform for Topological Quantum Computation Using Semiconductor Heterostructures, Phys. Rev. Lett. **104**, 040502 (2010).

[18] V. Mourik, K. Zuo, S. M. Frolov, S. R. Plissard, E. P. A. M. Bakkers, and L. P. Kouwenhoven, Signatures of Majorana fermions in hybrid superconductor-semiconductor nanowire devices, Science **336**, 1003 (2012).

[19] J. Cayao, E. Prada, P. San-Jose, and R. Aguado, SNS junctions in nanowires with spin-orbit coupling: Role of confinement and helicity on the subgap spectrum, Phys. Rev. B **91**, 024514 (2015).

[20] C.-K. Chiu, T. Machida, Y. Huang, T. Hanaguri, and F.-C. Zhang, Scalable Majorana vortex modes in iron-based superconductors, Sci. Adv. **6**, eaay0443 (2020).

[21] M. Li, G. Li, L. Cao, X. Zhou, X. Wang, C. Jin, C.-K. Chiu, S. J. Pennycook, Z., and H.-J. Gao, Ordered and tunable Majorana-zero-mode lattice in naturally strained LiFeAs, Nature (London) **606**, 890 (2022).

[22] B. Göhler, V. Hamelbeck, T. Z. Markus, M. Kettner, G. F. Hanne, Z. Vager, R. Naaman, and H. Zacharias, Spin selectivity in electron transmission through self-assembled monolayers of double-stranded DNA, Science **331**, 894 (2011).

[23] A.-M. Guo and Q.-F. Sun, Spin-Selective Transport of Electrons in DNA Double Helix, Phys. Rev. Lett. **108**, 218102 (2012).

[24] D. Mishra, T. Z. Markus, R. Naaman, M. Kettner, B. Göhler, H. Zacharias, N. Friedman, M. Sheves, and C. Fontanesi, Spin-dependent electron transmission through bacteriorhodopsin embedded in purple membrane, Proc. Natl. Acad. Sci. USA **110**, 14872 (2013).

[25] G.-F. Du, H.-H. Fu, and R. Wu, Vibration-enhanced spin-selective transport of electrons in the DNA double helix, Phys. Rev. B **102**, 035431 (2020).

[26] Y. Utsumi, O. Entin-Wohlman, and A. Aharony, Spin selectivity through time-reversal symmetric helical junctions, Phys. Rev. B **102**, 035445 (2020).

[27] Q. Qian, H. Ren, J. Zhou, Z. Wan, J. Zhou, X. Yan, J. Cai, P. Wang, B. Li, Z. Sofer, B. Li, X. Duan, X. Pan, Y. Huang, and X. Duan, Chiral molecular intercalation superlattices, Nature (London) **606**, 902 (2022).

[28] A.-M. Guo and Q.-F. Sun, Topological states and quantized current in helical organic molecules, Phys. Rev. B **95**, 155411 (2017).

[29] A.-M. Guo, P.-J. Hu, X.-H. Gao, T.-F. Fang, and Q.-F. Sun, Topological phase transitions of Thouless charge pumping realized in helical organic molecules with long-range hopping, Phys. Rev. B **102**, 155402 (2020).

[30] A. Yu. Kasumov, M. Kociak, S. Guéron, B. Reulet, V. T. Volkov, D. V. Klinov, H. Bouchiat, Proximity-induced superconductivity in DNA, Science **291**, 280 (2001).

[31] H. Alpern, E. Katzir, S. Yochelis, N. Katz, Y. Paltiel, and O. Millo, Unconventional superconductivity induced in Nb films by adsorbed chiral molecules, New J. Phys. **18**, 113048 (2016).

[32] T. Shapira, H. Alpern, S. Yochelis, T.-K. Lee, C.-C. Kaun, Y. Paltiel, G. Koren, and O. Millo, Unconventional order parameter induced by helical chiral molecules adsorbed on a metal proximity coupled to a superconductor, Phys. Rev. B **98**, 214513 (2018).

[33] H. Alpern, K. Yavilberg, T. Dvir, N. Sukenik, M. Klang, S. Yochelis, H. Cohen, E. Grosfeld, H. Steinberg, Y. Paltiel, and O. Millo, Magnetic-related states and order parameter induced in a conventional superconductor by nonmagnetic chiral molecules, Nano Lett. **19**, 5167 (2019).

[34] H.-Z. Tang, Q.-F. Sun, J.-J. Liu, and Y.-T. Zhang, Majorana zero modes in regular B-form single-stranded DNA proximity-coupled to an *s*-wave superconductor, Phys. Rev. B **99**, 235427 (2019).

[35] Q. Chen, A.-M. Guo, J. Liu, F. M. Peeters, and Q.-F. Sun, Topological phase transitions and Majorana zero modes in DNA double helix coupled to *s*-wave superconductors, New J. Phys. **23**, 093047 (2021).

[36] E. B. Sonin, Ballistic SNS sandwich as a Josephson junction, Phys. Rev. B **104**, 094517 (2021).

[37] A. Samoilenka, E. Babaev, Boundary states with elevated critical temperatures in Bardeen-Cooper-Schrieffer superconductors, Phys. Rev. B **101**, 134512 (2020).

[38] A. F. Volkov, A. Anishchanka, K. B. Efetov, Odd triplet superconductivity in a superconductor/ferromagnet system with a spiral magnetic structure, Phys. Rev. B **73**, 104412 (2006).

[39] A.-M. Guo and Q.-F. Sun, Spin-dependent electron transport in protein-like single-helical molecules, Proc. Natl. Acad. Sci. USA **111**, 11658 (2014).

[40] Q.-F. Sun, J. Wang, and T.-H. Lin, Resonant Andreev reflection in a normal-metal–quantum-dot–superconductor system, Phys. Rev. B **59**, 3831 (1999).

[41] S.-N. Zhang, W. Pei, T.-F. Fang, and Q.-F. Sun, Phonon-assisted transport through quantum dots with normal and superconducting leads, Phys. Rev. B **86**, 104513 (2012).

[42] Z. Yang, Q. Yang, J. Hu, and D. E. Liu, Dissipative Floquet Majorana Modes in Proximity-Induced Topological Superconductors, Phys. Rev. Lett. **126**, 086801 (2021).

[43] H. Pan and S. Das Sarma, Physical mechanisms for zero-bias conductance peaks in Majorana nanowires, Phys. Rev. Res. **2**, 013377 (2020).

[44] B. H. Wu and J. C. Cao, Tunneling transport through superconducting wires with Majorana bound states, Phys. Rev. B **85**, 085415 (2012).

[45] Q.-F. Sun and X. C. Xie, Quantum transport through a graphene nanoribbon-superconductor junction, J. Phys.: Condens. Matter **21**, 344204 (2009).

[46] A. R. Akhmerov, J. P. Dahlhaus, F. Hassler, M. Wimmer, and C. W. J. Beenakker, Quantized Conductance at the Majorana Phase Transition in a Disordered Superconducting Wire, Phys. Rev. Lett. **106**, 057001 (2011).

[47] M. M. Maśka, A. Gorczyca-Goraj, J. Tworzydło, and T. Domański, Majorana quasiparticles of an inhomogeneous Rashba chain, Phys. Rev. B **95**, 045429 (2017).

[48] D. S. Fisher and P. A. Lee, Relation between conductivity and transmission matrix, Phys. Rev. B **23**, 6851(R) (1981).

[49] S. Das Sarma, A. Nag, and J. D. Sau, How to infer non-Abelian statistics and topological visibility from tunneling conductance properties of realistic Majorana nanowires, Phys. Rev. B **94**, 035143 (2016).

[50] F. Kuemmeth, S. Ilani, D. C. Ralph, and P. L. McEuen, Coupling of spin and orbital motion of electrons in carbon nanotubes, Nature (London) **452**, 448 (2008).

[51] S. Das Sarma, J. D. Sau, and T. D. Stanescu, Splitting of the zero-bias conductance peak as smoking gun evidence for the existence of the Majorana mode in a superconductor-semiconductor nanowire, Phys. Rev. B **86**, 220506(R) (2012).

[52] R. G. Endres, D. L. Cox, and R. R. P. Singh, Colloquium: The quest for high-conductance DNA, Rev. Mod. Phys. **76**, 195 (2004).

[53] E. Katzir, N. Sukenik, Y. Kalcheim, H. Alpern, S. Yochelis, Y. A. Berlin, M. A. Ratner, O. Millo, and Y. Paltiel, Probing molecular-transport properties using the superconducting proximity effect, Small Methods **1**, 1600034 (2017).

[54] M. Z. Hasan and C. L. Kane, Colloquium: Topological insulators, Rev. Mod. Phys. **82**, 3045 (2010).

[55] M. R. Zirnbauer, Particle-hole symmetries in condensed matter, J. Math. Phys. **62**, 021101 (2021).

[56] D. Rainis, L. Trifunovic, J. Klinovaja, and D. Loss, Towards a realistic transport modeling in a superconducting nanowire with Majorana fermions, Phys. Rev. B **87**, 024515 (2013).

[57] C.-X. Liu, J. D. Sau, and S. Das Sarma, Distinguishing topological Majorana bound states from trivial Andreev bound states: Proposed tests through differential tunneling conductance spectroscopy, Phys. Rev. B **97**, 214502 (2018).

[58] C. Moore, T. D. Stanescu, and S. Tewari, Two-terminal charge tunneling: Disentangling Majorana zero modes from partially separated Andreev bound states in semiconductor-superconductor heterostructures, Phys. Rev. B **97**, 165302 (2018).

[59] S. Zhang, Z. Wang, D. Pan, H. Li, S. Lu, Z. Li, G. Zhang, D. Liu, Z. Cao, L. Liu, L. Wen, D. Liao, R. Zhuo, R. Shang, D. E. Liu, J. Zhao, and H. Zhang, Suppressing Andreev Bound State Zero Bias Peaks Using a Strongly Dissipative Lead, Phys. Rev. Lett. **128**, 076803 (2022).

[60] L. Fu and C. L. Kane, Probing Neutral Majorana Fermion Edge Modes with Charge Transport, Phys. Rev. Lett. **102**, 216403 (2009).

[61] R. M. Lutchyn, J. D. Sau, and S. Das Sarma, Majorana Fermions and a Topological Phase Transition in Semiconductor-Superconductor Heterostructures, Phys. Rev. Lett. **105**, 077001 (2010).

[62] M. Alvarado, A. Iks, A. Zazunov, R. Egger, and A. L. Yeyati, Boundary Green's function approach for spinful single-channel and multichannel Majorana nanowires, Phys. Rev. B **101**, 094511 (2020).

[63] A. Kobiałka, N. Sedlmayr, and A. Ptok, Majorana bound states in a superconducting Rashba nanowire in the presence of antiferromagnetic order, Phys. Rev. B **103**, 125110 (2021).

[64] X.-L. Qi and S.-C. Zhang, Topological insulators and superconductors, Rev. Mod. Phys. **83**, 1057 (2011).

[65] J. Alicea, Y. Oreg, G. Refael, F. von Oppen and M. P. A. Fisher, Non-Abelian statistics and topological quantum information processing in 1D wire networks, Nat. Phys. **7**, 412 (2011).

[66] Q. Yan and Q.-F. Sun, Realization of arbitrary two-qubit quantum gates based on chiral Majorana fermions, Chin. Phys. B **30**, 040303 (2021).